1140 Chem. Mater. 1995, 7, 1140−1152

Structural Investigation of Mercury-Intercalated Titanium Disulfide. 2. HRTEM of Hg_xTiS_2

M. Sidorov,[†] M. McKelvy,[*,†] R. Sharma,[†] W. Glaunsinger,[‡,†] P. Ganal,[§]
P. Moreau,[§] and G. Ouvrard[§]

Center for Solid State Science, Arizona State University, Tempe, Arizona 85287-1704; Department of Chemistry and Biochemistry, Arizona State University, Tempe, Arizona 85287-1604; and Institut des Matériaux de Nantes (I.M.N.), 2, rue de la Houssinière, 44072 Nantes, France

Received October 27, 1994. Revised Manuscript Received March 21, 1995[⊗]

The lowvalent nature of Hg in Hg_xTiS_2 ($Hg^{\delta+}$, where $\delta \ll 1$) has remarkable structural consequences that have been revealed by high-resolution transmission electron microscopy observations during the in situ deintercalation of $Hg_{1.24}TiS_2$. Hg guest layers and islands are comprised of one-dimensional Hg chains that are incommensurate with the host-layer sublattice along the chain-axis direction. Deintercalation induces a host-layer-stacking shift along the Hg chains, changing the coordination of the sulfur channels in which the chains reside from trigonal prismatic (TP) to distorted trigonal antiprismatic (DTAP). The resulting DTAP structure consists of interpenetrating *C*-face-centered monoclinic Hg and TiS_2 sublattices, with common *a* and *c* axes and incommensurate *b* axes. The 2-fold intralayer symmetry of the Hg layers, combined with the 3-fold intralayer symmetry of the host layers, results in the formation of three equivalent Hg sublattices with intralayer rotations of 120°. The chains exhibit substantial axial thermal disorder, which is enhanced during deintercalation. These compounds exhibit significant metallic guest−guest bonding, with an intrachain Hg−Hg distance of 2.76 Å and novel guest−host interactions between the Hg chains and sulfur channels, as evidenced by the intralayer off-chain-axis modulation of the Hg positions (±0.2 Å).

Introduction

Compounds formed by the intercalation of mercury into transition-metal dichalcogenides (TMDs) have many unusual features.[1−9] Unlike other metal−TMD intercalation compounds (M−TMDICs), these intercalates exhibit novel properties such as a thermally reversible intercalation process and essentially neutral guest species. Their guest−host interactions are best described as weakly covalent in nature, with very little ionic character. For example, the characteristically weak guest−host interactions in Hg_xTiS_2 follow from the similarity between its deintercalation enthalpy and the heat of vaporization of liquid Hg, both of which are 14 kcal/mol of Hg.[3] These interactions are especially weak compared to those typically found for M−TMDICs, where ionic guest−host interactions are generally present.[10,11]

Mercury is unusual in its ability to form chainlike polymetallic cations in a variety of compounds. Previously observed polymetallic cations include three-atom Hg_3^{2+} chains in the $Hg_3(AlCl_4)_2$ and $Hg_3(AsF_6)_2$ salts,[12,13] the four-atom Hg_4^{2+} chains in $Hg_4(AsF_6)_2$,[14] and the one-dimensional $(Hg^{1/3+})_\infty$ chains in $Hg_{3-\delta}MF_6$ (M = As, Sb, Ta and Nb).[15] However, cationic character is not essential to metallic Hg chain formation, as infinite, zerovalent Hg chains are found in β-Hg.[16] The possible formation of Hg chains in the lamellar Hg_xTiS_2 compounds provided the original motivation for detailed structural investigations of these materials.

X-ray powder and single-crystal diffraction studies of $Hg_{1.24}TiS_2$ presented in paper 1 show that this compound adopts an unusual (3 + 1)-dimensional misfit structure.[8] This structure can be considered as two interpenetrating Hg and TiS_2 sublattices, with each sublattice described by the monoclinic space group *C*2/

[†] Center for Solid State Science, ASU.

[‡] Department of Chemistry and Biochemistry, ASU.

[§] Institut des Matériaux de Nantes.

[⊗] Abstract published in *Advance ACS Abstracts,* April 15, 1995.

(1) Ong, E. W. Ph.D. Thesis, Arizona State University, Tempe, AZ, 1990.

(2) McKelvy, M.; Sharma, R.; Ong, E.; Burr, G.; Glaunsinger, W. *Chem. Mater.* **1991**, *3*, 783.

(3) Ong, E. W.; McKelvy, M. J.; Ouvrard, G.; Glaunsinger, W. S. *Chem. Mater.* **1992**, *4*, 14.

(4) Moreau, P.; Ouvrard, G. *Chemical Physics of Intercalation II*; Plenum Press: New York, 1993; Nato ASI Series Vol. 305, p 351.

(5) Ganal, P.; Olberding, W.; Butz, T.; Ouvrard, G. *Chemical Physics of Intercalation II*; Plenum Press: New York, 1993; Nato ASI Series Vol. 305, p 383.

(6) Moreau, P.; Ganal, P.; Ouvrard, G. *Mol. Cryst. Liq. Cryst.* **1994**, *244*, 325.

(7) McKelvy, M.; Sidorov, M.; Marie, A.; Sharma, R.; Glaunsinger, W. *Mater. Res. Soc. Symp. Proc.* **1994**, *332*, 115.

(8) Ganal, P.; Moreau, P.; Ouvrard, G.; Sidorov, M.; McKelvy, M.; Glaunsinger, W., *Chem. Mater.*, previous article in this issue.

(9) McKelvy, M.; Sidorov, M.; Marie, A.; Sharma, R.; Glaunsinger, W. *Chem. Mater.* **1994**, *6*, 2233, and in press.

(10) Lévy, F., Ed. *Intercalated Layered Materials*; D. Reidel: Dordrecht, Holland, 1979.

(11) Whittingham, M. S., Jacobson, A. J., Eds. *Intercalation Chemistry*; Academic Press: New York, 1982.

(12) Torsi, G.; Fung, K. W.; Begun, G. H.; Manatov, G. *Inorg. Chem.* **1975**, *10*, 2285.

(13) Cutforth, B. D.; Davies, C. G.; Dean, P. A. W.; Gillespie, R. J.; Ireland, P. R.; Ummat, P. K. *Inorg. Chem.* **1973**, *12*, 1343.

(14) Cutforth, B. D.; Gillespie, R. J.; Ireland, P. R.; Sawyer, J. F.; Ummat, P. K. *Inorg. Chem.* **1983**, *22*, 1344.

(15) Brown, I. D.; Datars, W. R.; Gillespie, R. J.; Morgan, K. R.; Tun, Z.; Ummat, P. K. *J. Solid State Chem.* **1985**, *57*, 34.

(16) Atoji, M.; Schirber, J. E.; Swendson, C. A. *J. Chem. Phys.* **1959**, *31*, 1628.

0897-4756/95/2807-1140$09.00/0

m. The sublattices share commensurate *a* and *c* axes but are incommensurate along their common *b* axis, as indicated by the cell parameters $a = 5.9223(9)$ Å, $b_{TiS_2} = 3.4076(2)$ Å, $b_{Hg} = 2.7566(1)$ Å, $c = 8.862(1)$ Å, and $\beta = 102.33(3)°$. The TiS_2 layers in $Hg_{1.24}TiS_2$ have shifted with respect to each other by (2/3)*a* along their monoclinic *a* axis relative to their octahedral stacking arrangement in TiS_2. This restacking results in near-trigonal prismatic coordination of the guest sites, which produces a network of linear sulfur channels rotated by 120° with respect to each other in the van der Waals (vdW) gap. The intercalated Hg atoms form infinite chains that occupy these relatively open sulfur channels, with the intrachain Hg–Hg distance (2.757 Å) being much smaller than the interchain Hg–Hg distance (3.267 Å). A comparison of the intrachain Hg–Hg distance in $Hg_{1.24}TiS_2$ to those determined for other Hg-chain-containing compounds with known ionic character indicates that the intercalated Hg in the former compound has very little ionic character.[8]

The structural studies in paper 1[8] also indicated the presence of intrinsic structural imperfections that were not incorporated into the refinement. The technique of choice for the detailed investigation of such defects is high-resolution transmission electron microscopy (HRTEM). In this paper (2), we use in situ HRTEM to follow the structural evolution of mercury-intercalated titanium disulfide during Hg deintercalation and to identify and determine the structure of the associated structural imperfections and modulations.

Experimental Section

Stage-1 $Hg_{1.24}TiS_2$ was prepared by direct reaction of exact ratios of high-purity Hg and TiS_2 (1.24:1.00) at 593 K followed by slow cooling to ambient temperature, as reported previously.[1-3] The Hg was triply distilled (<5 ppm foreign metals), and highly stoichiometric titanium disulfide, $Ti_{1.002}S_2$, was used as the host.[17] The host composition was confirmed by oxidative thermogravimetric analysis (TGA) and X-ray powder diffraction (XPD) analysis of its *c*-lattice parameter.[17,18] Exact sample compositions were confirmed by TGA of the quantitative Hg deintercalation process under an Ar atmosphere and were found to be $Hg_{1.24\pm0.01}TiS_2$.[3]

TEM samples were prepared by first cooling the polycrystalline $Hg_{1.24}TiS_2$ samples to 77 K in an agate mortar and pestle immersed in liquid nitrogen inside a nitrogen-atmosphere glovebox. The samples were crushed while under liquid nitrogen, warmed to ambient temperature, and then dispersed onto holey carbon-coated grids. The resulting crystal fragments were thin (often platelike) and well suited for TEM observation. XPD and TGA were used to verify that no significant structural or compositional change occurred during the TEM specimen preparation process.[2,3,7,9]

The TEM observations were made under ambient conditions using Topcon 002B (200 kV, spherical aberration coefficient (C_s) ≈ 0.4 mm and point-to-point resolution of 1.8 Å) and JEOL 4000FX (400 kV, $C_s \approx 1.2$ mm and point-to-point resolution of 1.7 Å) transmission electron microscopes. Upon introduction into the microscope vacuum, the samples inherently begin to deintercalate Hg, so that all of the samples studied have undergone some Hg deintercalation. Additional deintercalation was induced by electron-beam heating.

The TEM crystals were most often found with their layers oriented perpendicular to the electron beam. These crystals still required some tilting to align their *c* axes with the electron beam, suggesting the intercalate *c* axis was slightly off the perpendicular to the host layers. The *c*-axis studies were complemented by *a*- and *b*-axis investigations to elucidate the intercalate crystal structure.

The diffraction patterns recorded in these studies were calibrated using pure TiS_2 as a diffraction standard. ⟨110⟩ images of Si were used as a calibration standard to determine the *d* spacings in the Fourier transforms of HRTEM images using the lattice vector measurement technique.[19] Image processing was performed using an image analysis system based on a Gatan Digital Micrograph software application package installed on a Quadra 950 Macintosh computer. This package provides many tools for analysis and processing of HRTEM images, including Fourier filtering.[20] HRTEM images were simulated via the multislice approach[21,22] of dynamic diffraction theory using an EMS software package[23] installed on a Silicon Graphics workstation.

Results and Discussion

In-Plane Structure. The microcrystals observed by TEM either had no distinct form or a hexagonal shape. As expected for a lamellar material, the crystals were most often found oriented with their layers perpendicular to the electron beam. However, small crystals could readily be found that were oriented with their lamella oriented parallel to the electron beam.[2,7,9]

A relatively high activity of Hg vapor is required over the intercalates at ambient temperature to maintain the fully intercalated composition $Hg_{1.24}TiS_2$. As mentioned earlier, all of the samples experienced some deintercalation from the original $Hg_{1.24}TiS_2$ composition upon ambient-temperature exposure to the microscope vacuum. This typically resulted in a small percentage of guest galleries exhibiting some partial or occasionally complete deintercalation prior to observation. Additional deintercalation occurred due to, and was purposely induced by, electron-beam heating during the electron microscope observations. The local compositions of the intercalate regions observed by HRTEM were difficult to determine accurately, in part due to the dynamic nature of the Hg deintercalation process, which often occurred unintentionally, as well as intentionally, during the structural observations. Also, the Hg compositions of the HRTEM-observed regions often varied dramatically from layer to layer within the regions due to the presence of neighboring intercalated and deintercalated guest galleries. The approximate composition of the regions investigated parallel to their layers was estimated from the ratio of intercalated and deintercalated guest galleries in the region of interest. Each gallery or area of a gallery containing a guest layer was assumed to have a local Hg_xTiS_2 composition in the range $1.00 \le x \le 1.24$, consistent with the composition range of pure stage-1 Hg_xTiS_2 ($1.00 \le x \le 1.24$).[3] For crystals viewed along their *c* axes, the compositions of the regions of interest were determined by comparing calculated and experimental images as a function of Hg composition. Care was taken to avoid regions containing Hg guest islands in the imaging studies in order to optimize sample homogeneity in the regions used for image comparison. The *c*-axis image comparison results

---

[17] McKelvy, M. J.; Glaunsinger, W. S. *J. Solid State Chem.* **1987**, *66*, 181.

[18] Thompson, A. H.; Gamble, F. R.; Symon, C. R. *Mater. Res. Bull.* **1975**, *10*, 915.

[19] de Ruijter, W. J.; Sharma, R.; McCartney, M. R.; Smith, D. J. *Ultramicroscopy*, in press.

[20] Russ, J. C. *The Image Processing Handbook*; CRC Press: Boca Raton, FL, 1992.

[21] Cowley, J. M.; Moodie, A. F. *Acta Crystallogr.* **1957**, *10*, 609.

[22] Ishizuka, K.; Uyeda, N. *Acta Crystallogr.* **1977**, *A33*, 740.

[23] Stadelmann, P. A. *Ultramicroscopy* **1987**, *21*, 131.

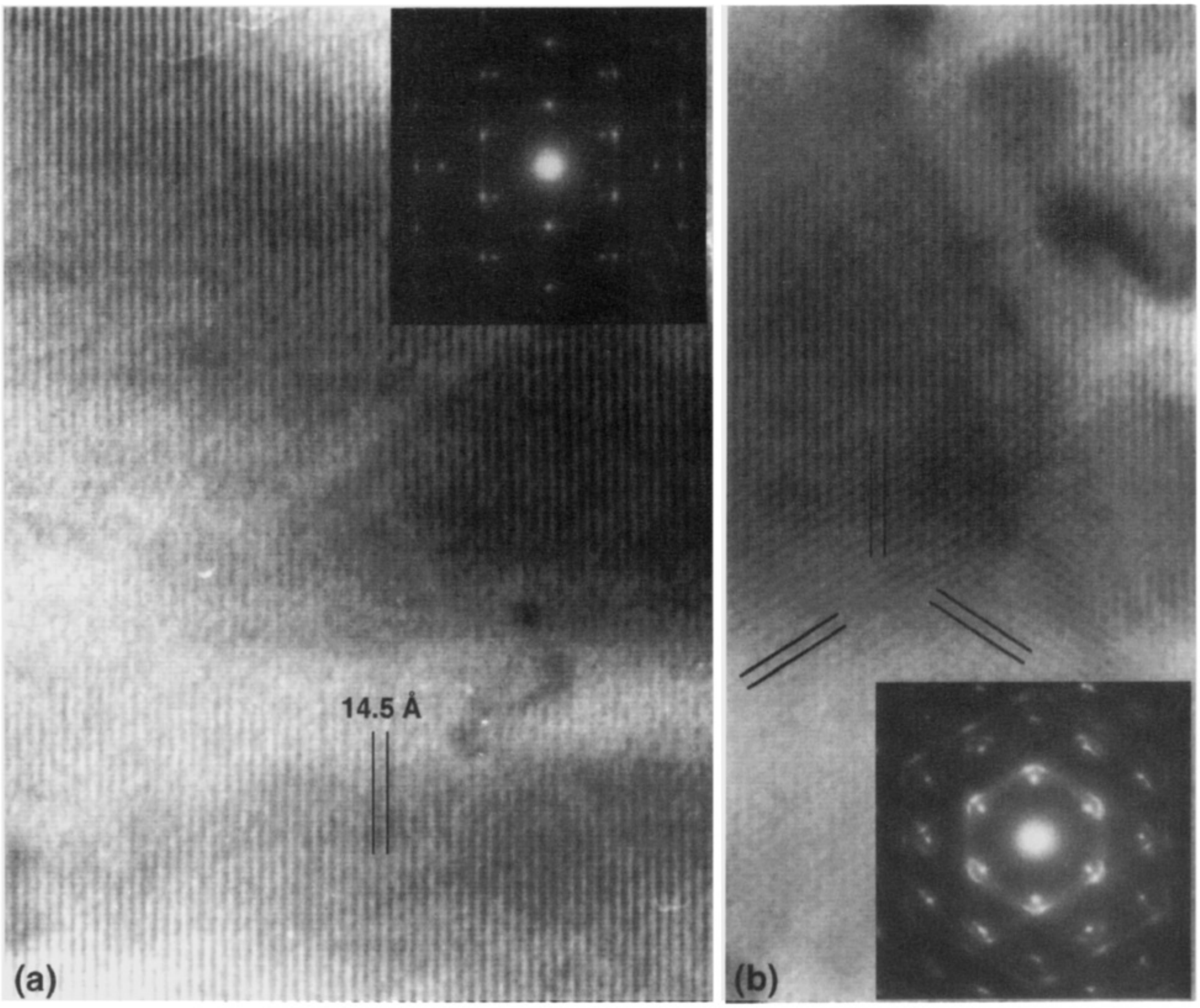

Figure 1. Multibeam, bright-field TEM images and associated SAD patterns of Hg_xTiS_2 viewed along *c*. Well-ordered Hg and TiS_2 sublattices produce distinct Moiré fringes of ~14.5 Å spacing in the images. (a) Thin (~100 Å) region of a crystal showing one-dimensional Moiré character. (b) Thicker (~500 Å) crystal region showing three sets of Moiré fringes rotated by 120° with respect to each other. The parallel black lines highlight the ~14.5 Å Moiré spacings in both images.

presented herein are for regions of guest galleries that are intercalated within the area of the crystal observed by HRTEM. However, the area outside of the field of view typically contained on occasional partially empty gallery in the vicinity of the area observed. Selected-area diffraction (SAD) was used to study Hg_xTiS_2 throughout the deintercalation process. Unless otherwise noted, the general formula Hg_xTiS_2 will be used to describe the variable Hg composition of the samples studied herein. It is also important to note the samples studied herein are inherently nonequilibrium in nature, as they are not observed at thermal equilibrium during the course of the deintercalation process.

All of the Hg_xTiS_2 samples exhibited well-ordered sublattices that produce distinct Moiré patterns in multibeam, bright-field TEM images and an array of extra spots in their corresponding selected area diffraction (SAD) patterns when viewed down their *c* axes, as shown in Figure 1. The appearance of the Moiré patterns depends on the thickness of the region of the sample being imaged. In relatively thin regions, Moiré fringes having a spacing of approximately 14.5 Å were observed in only one direction, as shown in Figure 1a. In thicker regions, a hexagonal Moiré network is found. This network is composed of three sets of fringes with the same spacing that are rotated by 120° with respect to each other, as illustrated in Figure 1b.

Figure 2a–c shows the typical (*hk*0) SAD patterns of Hg_xTiS_2 in more detail. For comparison, a pattern taken from pristine TiS_2 is shown in Figure 2d. The most common type of (*hk*0) SAD pattern for thin (~100 Å) Hg_xTiS_2 regions is shown together with its schematic representation in Figure 2a,b. The observed reflections in this complicated pattern can be interpreted as arising from the superposition of partially commensurate monoclinic TiS_2 and mercury sublattices. The TiS_2 sublattice produces the nearly hexagonal (*hk*0) subset of reflections, which correspond to the observed reflections $d_{200} = 2.94 \pm 0.01$ Å, $d_{110} = 2.95 \pm 0.01$ Å and $d_{020} = 1.70 \pm 0.01$ Å, whereas the Hg sublattice gives rise to the reflections $d_{200} = 2.94 \pm 0.01$ Å, $d_{110} = 2.51 \pm 0.01$ Å, and $d_{020} = 1.38 \pm 0.01$ Å. The (200) reflections of the host and guest sublattices are superimposed, which is why the relative intensities of these reflections are significantly higher than those for pristine TiS_2, as shown in Figure 2d. These *d* spacings are all within experimental error of those observed for the monoclinic TiS_2 and Hg sublattices in $Hg_{1.24}TiS_2$, with one notable

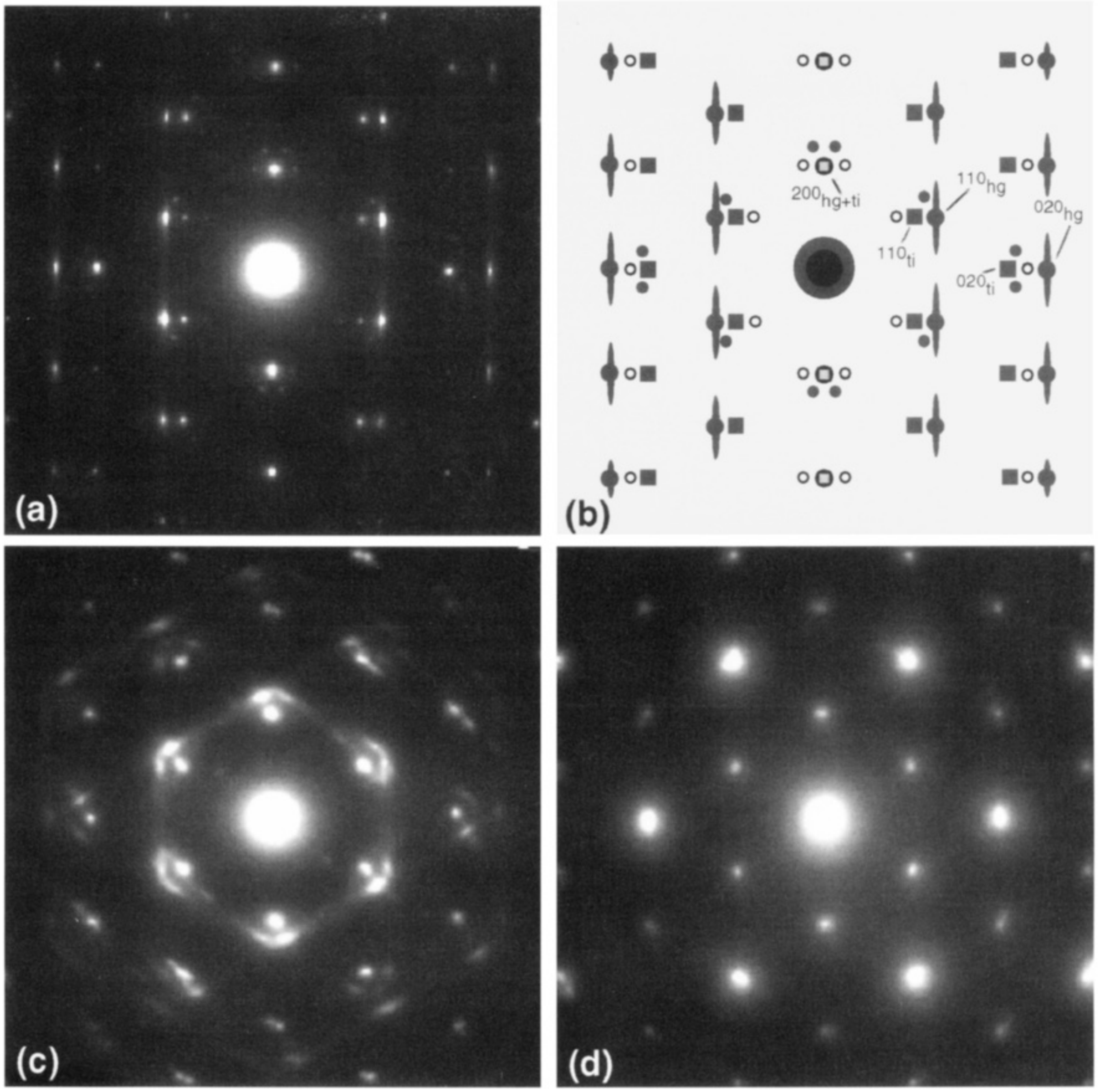

Figure 2. Typical SAD patterns obtained along *c*. (a) SAD pattern from a thin region of the Hg_xTiS_2 crystal shown in Figure 1a. (b) Schematic representation of the pattern shown in (a). The hexagonal set of reflections generated by the TiS_2 sublattice are shown as squares (■). The partially commensurate set of reflections generated by the three equivalent Hg sublattices rotated by 120° relative to each other are given by the large and small filled circles (●, ·). The small filled circles represent the Hg reflections arising from the two Hg orientations present in minor amounts, whereas the large filled circles correspond to the major orientation. The (200) reflections of the TiS_2 and major Hg sublattices are superimosed along the commensurate a^* axis (indicated by $200_{\mathrm{Hg+Ti}}$), while their sublattice patterns are incommensurate along b^*. The array of extra spots shown as small open circles (○) can arise from double diffraction. However, as discussed later in the text, *a*-axis modulation of the Hg positions can also contribute to these reflections. The diffuse streaks accompanying the Hg reflections indicate the presence of correlated atomic displacements of the Hg sublattice along *b*. Selected reflections associated with the TiS_2 and Hg sublattices are indicated by Ti and Hg, respectively. (c) Typical SAD pattern from a thicker region of the Hg_xTiS_2 crystal showing equal amounts of all three orientational variants of the Hg sublattice. Note there are now three sets of diffuse streaks in the Hg reciprocal lattice rotated by 120° with respect to each other. (d) SAD pattern for TiS_2.

exception. The 2.94 Å spacing for d_{200} is significantly greater than that observed by X-ray powder diffraction for $Hg_{1.24}TiS_2$ (2.89 Å), suggesting either a slight decrease in β or an increase in a occurs during partial Hg deintercalation. The nearest coincidence, but not exact matching, of the (020) reflections occurs for $25\cdot[d_{020}(TiS_2)]$ and $31\cdot[d_{020}(Hg)]$. As a result, the in-plane Hg and TiS_2 sublattices share a commensurate *a* axis but are incommensurate along their *b* axes. In addition to the reflections that solely originate from the TiS_2 and Hg sublattices, there are extra spots that can arise from double diffraction. However, these extra reflections can also be associated with local modulation of the Hg positions, as discussed later. Further examination of Figure 2a,b also reveals the presence of two additional subsets of relatively weak secondary reflections having the same symmetry as those arising from the Hg sublattice but rotated by 120° and 240° relative to the stronger Hg sublattice reflections. These additional reflection subsets together with the first indicate the presence of three equivalent Hg sublattices that differ only by their orientation relative to each other. This is confirmed by SAD patterns from thicker crystals, as shown in Figure 2c, which routinely contain the three subsets of Hg reflections with similar intensities. Although sample heating by prolonged electron-beam

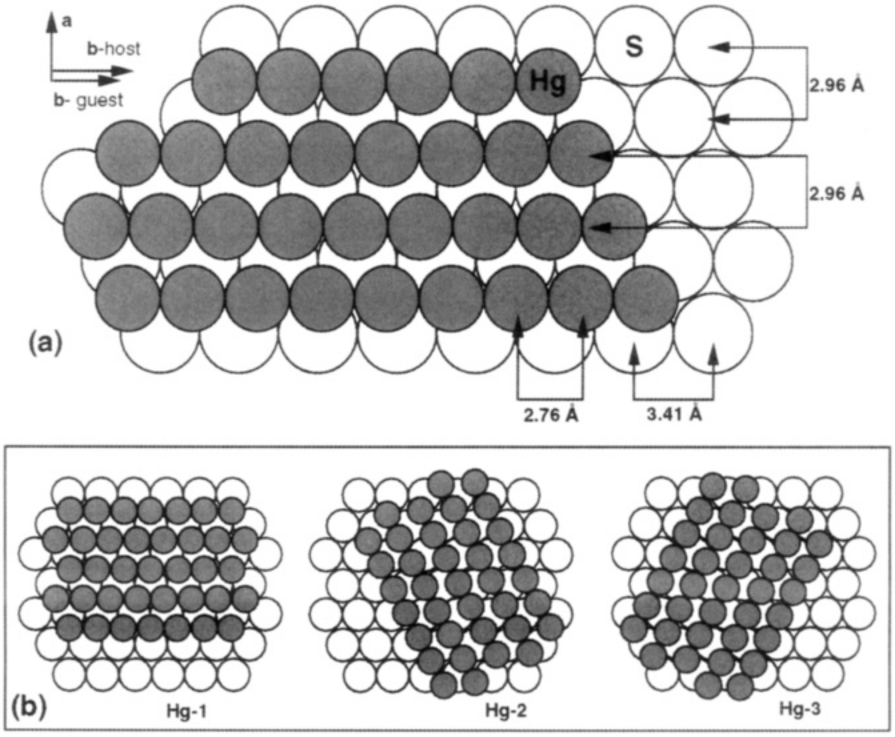

Figure 3. (a) Model of the in-plane structure of Hg_xTiS_2 viewed perpendicular to layers showing the formation of partially commensurate Hg guest layers for a single Hg sublattice orientation. The Hg layers are composed of infinite chains of atoms aligned along the incommensurate b direction midway between neighboring sulfur rows. (b) Model showing the three equivalent orientational variants of Hg with respect to the host layers occupying different guest galleries.

exposure resulted in Hg deintercalation and correspondingly lower Hg peak intensities, the symmetry of the SAD patterns for thin and thick regions was the same over a wide range of composition. Therefore, these patterns are characteristic of Hg_xTiS_2 during the deintercalation process.

The $(hk0)$ mercury reflections in these patterns where $k \neq 0$ are easily recognized by the presence of diffuse streaks along the a^* direction, which can be associated with defects in the Hg sublattice. The appearance of these streaks corresponds to correlated atomic displacements in the Hg sublattice along the b-axis direction.[24,25] The streaks become much more pronounced with extended electron-beam exposure and diminish substantially with reduced beam exposure, indicating that the corresponding disorder can be thermally driven by electron-beam heating.

Figure 3a presents a possible in-plane Hg arrangement corresponding to the observed SAD patterns, which is later confirmed by high-resolution lattice imaging. The mercury atoms form two-dimensional sheets in completely intercalated Hg_xTiS_2 guest layers or islands with a formal intercalate composition of $x = 1.24$. Each layer or island is composed of continuous Hg chains occupying the channels between the neighboring sulfur rows of the host TiS_2 when viewed perpendicular to the layers. The infinite Hg chains formed in this structure have a Hg−Hg distance of 2.76 Å along the chain axis, as shown in Figure 3a. These chains bear a strong similarity to the infinite Hg chains that form in β-Hg.[16] The intrachain Hg−Hg distance in Hg_xTiS_2 is actually somewhat shorter than the intrachain Hg−Hg distance of 2.825 Å found in the β-Hg structure,[16] which indicates significant metallic intrachain bonding occurs between the guests in Hg_xTiS_2. Although the chains are separated by 2.96 Å, the distance between Hg atoms in adjacent chains is 3.27 Å, so that the intrachain Hg−Hg interaction dominates the guest−guest interactions in Hg_xTiS_2. A more complete discussion of bonding in $Hg_{1.24}TiS_2$ is given in paper 1.[8] It is also noteworthy that streaking in the a^* direction in the SAD patterns can be directly related to Hg chain stacking faults and thermally induced motion of the Hg chains along b, as discussed above.

Due to the 3-fold, in-plane symmetry of the host layers and the 2-fold symmetry of the guest sheets, individual mercury layers or islands can have three equivalent orientations with respect to the host, as shown in Figure 3b. Having more than one orientation in the same gallery, especially for the small crystals investigated in this study, is a relatively unstable configuration due to inefficient guest packing and increased strain energy. However, all three orientations could exist in different guest galleries, especially if guest layers of like orientation are grouped together, with minimal effect on the free energy of the intercalate. Therefore, in relatively thin crystals that contain only a small number of intercalate layers, it is possible for only one orientation to be predominant, as shown, for example, in Figure 2a. However, all three orientations of the chains may be present in equal concentrations in thicker regions of crystals containing many intercalate layers. This expectation is confirmed by the $(hk0)$ SAD patterns observed for relatively thick crystals (~500 Å), which routinely contain three sets of equally intense Hg sublattice reflections rotated by 120° with respect to

---

(24) Cowley, J. M. *Diffraction Physics*; North-Holland: Amsterdam, 1975.

(25) Amoros, J. L.; Amoros, M. *Molecular Crystals Their Transforms and Diffuse Scattering*; John Wiley and Sons Inc.: New York, 1968; p 339.

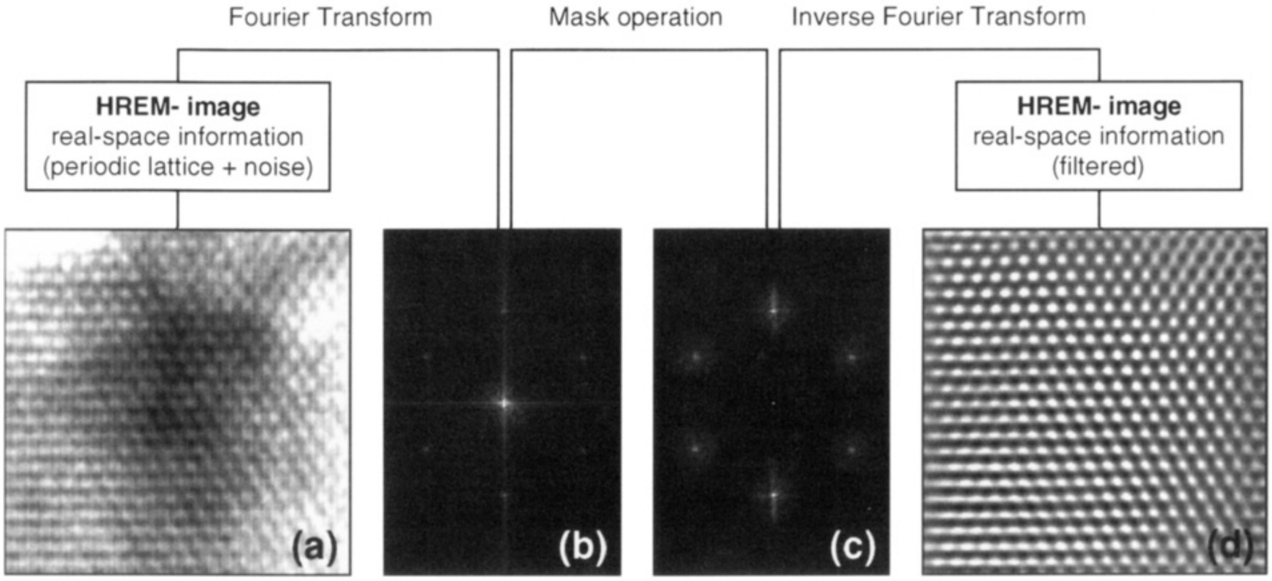

Figure 4. Main steps of Fourier filtering. (a) Experimental HRTEM image showing the periodic lattice and background noise. (b) Fourier transform of the image. The hexagonal set of peaks represents the periodic component of the image. The diffuse scattering around the central spot is a low-frequency component of the image arising from the nonperiodic background. The two orthogonal streaks visible in the transform are artifacts of the rectangular shape of the processed image. (c) The Fourier transform after applying the mask. In the case shown, the mask procedure retains the structural information close to the peaks and discards the rest. (d) The image after inverse Fourier transformation showing significant noise reduction.

each other, as seen in Figure 2c. In the multibeam, bright-field (*hk*0) HRTEM images shown in Figure 1, long-range modulations with a periodicity of approximately 14.5 Å are present along the incommensurate *b* direction shared by the TiS_2 sublattice and each Hg sublattice. The mutual alignment of the TiS_2 sublattice with one orientation of the Hg sublattice produces an example of pure "parallel" Moiré contrast, whose period of modulation can be estimated as

$$D = (d_{010}(\mathrm{TiS_2}))(d_{010}(\mathrm{Hg}))/(d_{010}(\mathrm{TiS_2}) - d_{010}(\mathrm{Hg})) = 14.5\ \text{Å}^{26} \quad (1)$$

Thus, each Hg sublattice orientation can generate a parallel Moiré contrast with a spacing of ~14.5 Å. This results in the observed parallel Moiré contrast, with 14.5 Å spacing, for thin crystals or regions in which a single Hg sublattice orientation is dominant, as observed in Figure 1a. For relatively thick crystals containing similar amounts of the three Hg sublattice orientations, a hexagonal Moiré network of 14.5 Å spacing is formed, as shown in Figure 1b. The thickness dependence of the Moiré contrast indicates that the different Hg sublattice orientations are primarily found in different guest layers, with a preference for layers with the same orientation to be grouped together.

To confirm and extend the above results, HRTEM image processing using the Fourier filtering technique was applied.[20] Figure 4 illustrates the main steps used in this analytical approach. First, a region of an experimental HRTEM image containing periodic components and random noise is digitized to an array of up to 640 × 480 pixels, as shown in Figure 4a. Next, fast Fourier transforms (FFTs) of areas of these images up to 256 × 256 pixels are performed to give patterns analogous to traditional "optical" diffractograms, as depicted in Figure 4b. Generally, FFT patterns of such small regions generate the same kind of diffraction data that SAD patterns do, but provide structural insight on a much smaller scale. A mask procedure was then applied to discard the regions exhibiting only diffuse scattering, as depicted in Figure 4c, followed by an inverse FFT to yield the real space image illustrated in Figure 4d. The Fourier filtering technique effectively eliminates most of the noise that is present in experimental images. Moreover, by using only one set of Fourier peaks and filtering out all other contributions to the FFT, it is possible to deconvolute complex images that arise from the superposition of two or more lattices into their constituent parts. In particular, this procedure was employed to deconvolute the images of the different orientations of the Hg sublattice and the TiS_2 sublattice.

Figure 5 shows a digitized (*hk*0) HRTEM image of Hg_xTiS_2 as well as FFTs taken from different parts of the image that correspond to thin and thick regions of the crystal. It is evident that the FFTs display the same behavior as SAD patterns, i.e., they show only one mercury orientation for the thinnest region close to the edge of a crystal, but all three orientations for a thicker region.

Figure 6a shows a higher-magnification experimental (*hk*0) image of a relatively thin crystal region after Fourier filtering to eliminate background noise. The image shows a long-range, one-dimensional modulation of the lattice of ~14.5 Å, consistent with one Hg sublattice orientation (Hg-1) being predominant and making the primary contribution to the image. The other two Hg sublattice orientations (Hg-2 and Hg-3) are present in only minor amounts, as evidenced by their relatively weak FFT intensities. The amplitudes of the corresponding Hg peaks in the FFT of this image and, therefore, the volume fractions of the different Hg orientations are in the ratio 4:1:1 for Hg-1, Hg-2, and Hg-3, respectively. Figure 6b–e shows the Fourier

---

(26) Hirsh, P.; Howie, A.; Nicholson, R. B.; Pashley, T. W.; Whelan, M. J. In *Electron Microscopy of Thin Crystals*, 2nd ed.; Hirsh, P., et al., Eds.; Robert E. Krieger: Malabar, 1977; p 169.

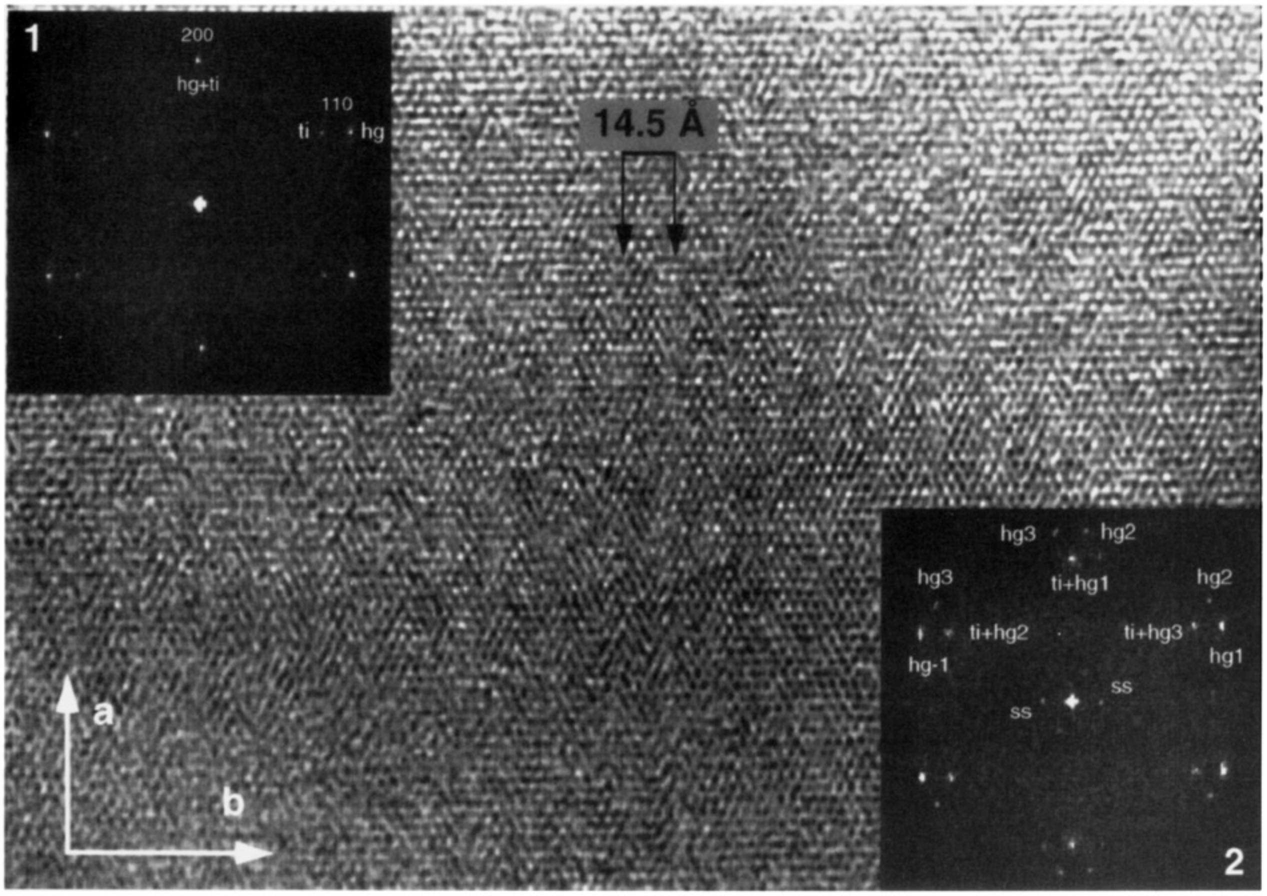

Figure 5. HRTEM image of Hg_xTiS_2 along *c*. Note the long-range lattice modulation of ~14.5 Å along *b*. (1) FFT obtained from the thin region at the top of the image containing a single Hg sublattice orientation. Selected host sublattice reflections are indicated by "Ti". Selected Hg-sublattice peaks are indicated by "Hg". The (200) reflections of both sublattices are superimposed. (2) FFT obtained from the thicker region at the bottom of the image. Selected reflections corresponding to the three different Hg sublattice orientations present are marked as "Hg1", "Hg2", "Hg3" and produce the three sets of reflections rotated by 120° with respect to each other. Selected host sublattice reflections are again indicated by "Ti". The set of reflections marked as "ss" close to the central spot show the long-range modulation of the lattice of ~14.5 Å in three different directions. Note the similarity of the FFT patterns to the SAD patterns in Figure 2a,c.

components corresponding to the TiS_2 sublattice and the three Hg sublattice orientations that are extracted from the region shown in Figure 6a. A two-dimensional intralayer unit cell for each sublattice is outlined in its corresponding image. The results of Fourier filtering show directly the nearly 3-fold symmetry of the host and the chainlike structure of the Hg layers for the three Hg sublattice orientations, thus providing strong evidence for the proposed intralayer structural model.

Crystal Structure. Our HRTEM observations of crystals with their layers oriented parallel to the electron beam confirm the interlayer expansion of 2.95 ± 0.05 Å observed in previous studies for the Hg intercalation of TiS_2.[1-4,6,7] As for $Hg_{1.24}TiS_2$,[8] the observed intercalate structure can be described by monoclinic TiS_2 and Hg sublattices. However, as discussed earlier, there is a slight increase in d_{200} for both sublattices, suggesting that an increase in *a* or a decrease in β occurs during partial Hg deintercalation. An increase in *a* (0.1 Å) accounting for the increase in d_{200} would require an unlikely *a* axis host-layer expansion which is 6 times larger than observed for $Hg_{1.24}TiS_2$.[8] Furthermore, XPD refinements of the cell parameters of eleven different compositions throughout the stage-1 ($1.24 \geq x \geq 1.00$) phase region of Hg_xTiS_2 showed *a* to be independent of both composition and preparation method and equal to 5.922 ± 0.004 Å,[27] consistent with earlier XPD observations.[3] Although these samples are not undergoing dynamic deintercalation as those studied in the electron microscope, it is clear the composition of intercalated layer regions has little effect on *a*. However, a host-layer stacking shift resulting in a reduction in β can reasonably account for the observed pattern. The new value of β can be estimated directly from *c*-axis SAD patterns using the *a* lattice parameter for stage-1 Hg_xTiS_2, assuming it has the same degree of intralayer *a*-axis distortion as partially deintercalated $Hg_{1.24}TiS_2$, and the formula

$$\beta = \arcsin[d_{200}(Hg_xTiS_2)/(a/2)Hg_{1.24}TiS_2] = \arcsin(2.94 \pm 0.01\ \text{Å}/2.96\ \text{Å}) = 97 \pm 2^\circ \quad (2)$$

This suggests sublattice unit cells which differ significantly from the $\beta = 102^\circ$ monoclinic sublattice cells found for $Hg_{1.24}TiS_2$.[8] The origin of this difference is explained below.

Upon intercalation, many TiS_2 intercalation compounds restack from the octahedral coordination of the guest sites in TiS_2 to adopt a 3R structure characterized by a stacking sequence AbC CaB BcA that provides

---

[27] Moreau, P. Ph.D. Thesis, University of Nantes, Nantes, France, 1994.

[28] Friend, R. H.; Yoffe, A. D. *Adv. Phys.* **1987**, *36*, 14.

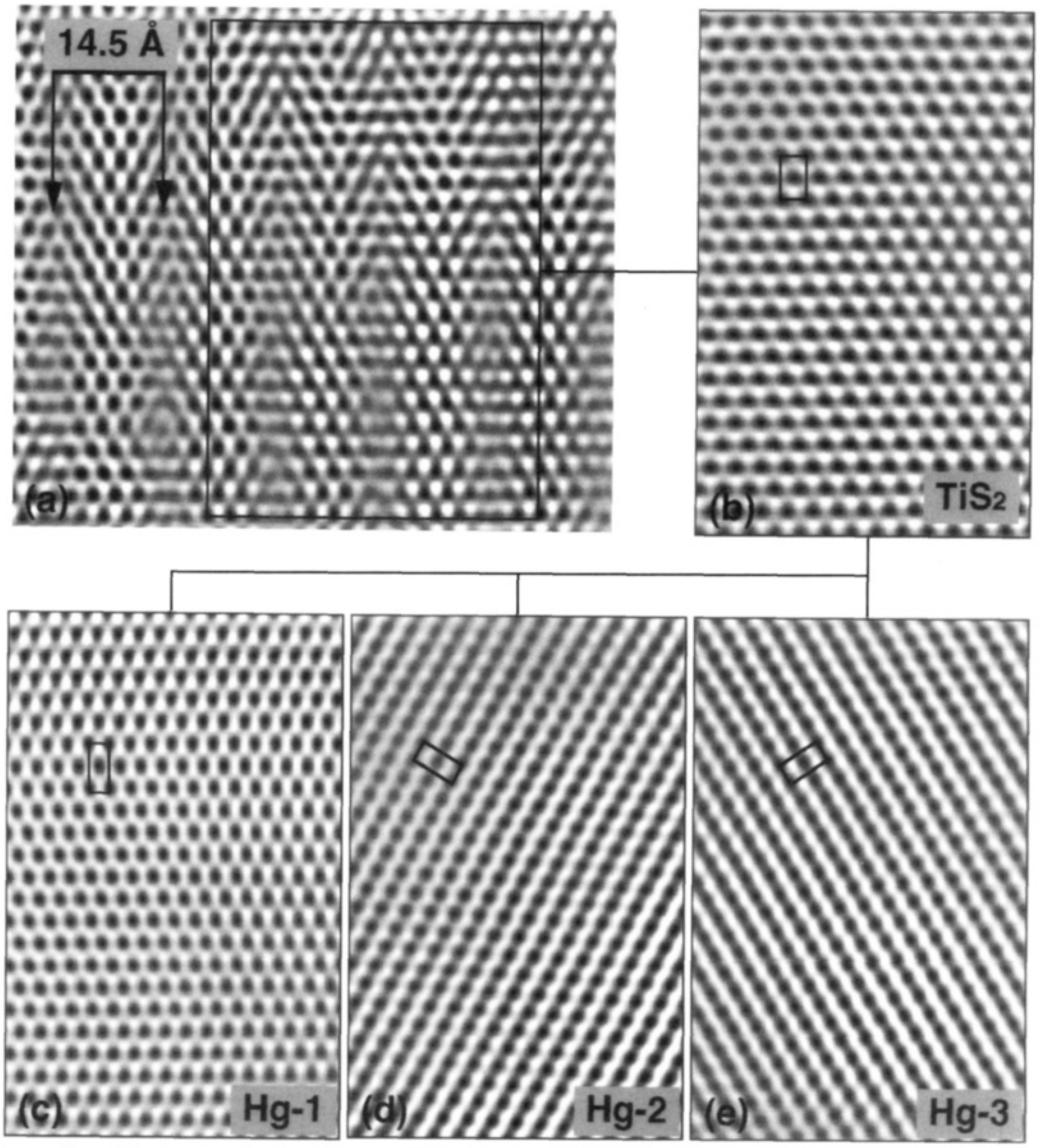

Figure 6. Separation of the host and Hg sublattices by Fourier image processing incorporating only the Bragg peaks associated with these sublattices. (a) Fourier-filtered HRTEM image along *c*, after the background noise has been filtered out, showing the long-range modulation of the lattice. (b) TiS_2 sublattice extracted from the FFT of the image in (a). (c–e) The three orientational variants of the Hg sublattice extracted from the FFT of the image in (a). Intralayer sublattice unit cells are outlined in images (b–e). The TiS_2 sublattice unit cell in (b) is for the Hg-1 orientation.

trigonal prismatic sites in the vdW gap.[10,11,28] With the exception of a minor structural distortion, this is the stacking arrangement found for $Hg_{1.24}TiS_2$.[8] The components of the restacking process can be understood by referring to Figure 7. In addition to the component involving the expansion of the host lattice perpendicular to the layers, depicted by the transition from Figure 7a to Figure 7b, restacking also involves a shear transformation component in which the TiS_2 layers shift relative to each other by $(1/3)a$ from the expanded cell shown in Figure 7b. The shear component of the restacking process is illustrated by the progression from Figure 7b to Figure 7c. This results in the formation of trigonal prismatic sulfur channels in which the incommensurate Hg sublattice chains are embedded. The TiS_2 host-layer structure remains largely unchanged by the intercalation process, as it generally does for reversible intercalation processes, leading to the $\beta = 102°$ monoclinic lattice found for $Hg_{1.24}TiS_2$.[8]

Trigonal prismatic coordination of the vdW gap is not the only stacking arrangement that can readily accommodate infinite Hg chains in the guest layers. Any shift of the host layers relative to each other along the *b* axis from the trigonal-prismatically coordinated guest layers shown in Figure 7c for $Hg_{1.24}TiS_2$ can also accommodate linear Hg chains. In particular, the distorted trigonal-antiprismatic (DTAP) coordination of the sulfur channels created by an interlayer shift of the host layers by $(1/2)b_{TiS_2}$ from the TP coordination shown in Figure 7c presents an alternative low-energy stacking arrangement around the Hg chains. The formation of such channels with DTAP coordination can also be viewed as an interlayer displacement of $(1/6)a$ relative to the octahedral guest-layer coordination of pristine TiS_2 or an interlayer displacement of $(1/2)a$ relative to the TP coordination in Figure 7c. This host-layer stacking arrangement results in a monoclinic TiS_2 sublattice unit cell having $\beta = 96.5°$, as shown in Figure 7d. The

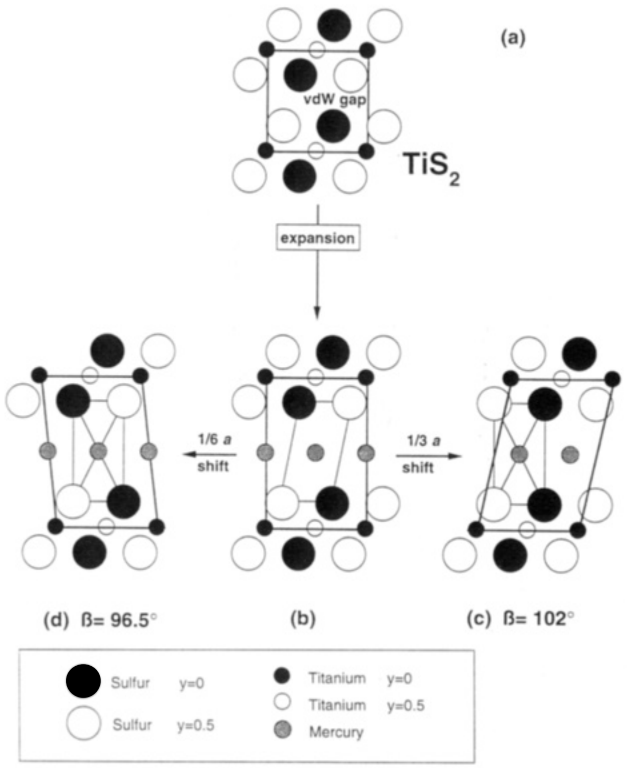

Figure 7. (a) Schematic diagram of the host TiS$_2$ structure along its pseudomonoclinic *b* axis. (b) Depiction of the component of the Hg intercalation process involving only the simple expansion of the lattice perpendicular to its layers shown along its pseudomonoclinic *b* axis. An additional shear component results in host-layer restacking during intercalation to provide the most suitable atomic arrangement for intercalated Hg chains. (c) The $\beta = 102°$ structure with trigonal prismatic coordination of the Hg chains achieved by an additional interlayer shift of the host layers by (1/3)*a* along the pseudomonoclinic *a* axis of the structure in (b). (d) The $\beta = 96.5°$ structure containing distorted trigonal antiprismatic coordination of the Hg chain achieved by an oppositely directed interlayer shift of the host layers by (1/6)*a* from the structure in (b). The $\beta = 102°$ and the $\beta = 96.5°$ structures are related by an interlayer shift of (1/2)*b* along the Hg chain-axis direction. They are also related by the (1/2)*a* interlayer displacement between Figure 7c,d.

atomic coordinates as well as the unit-cell parameters for this structure are given in Table 1.

The structure of the Hg$_x$TiS$_2$ intercalates was further explored by comparing computer simulations of HRTEM images with experimental images. Unfortunately, the EMS software package used for the simulations is not capable of treating incommensurate structures directly.[23] However, as mentioned earlier, a satisfactory coincidence along the incommensurate *b*-axis direction occurs for 25 and 31 unit cells of the TiS$_2$ and Hg sublattices, respectively. Thus, a structural unit of the combined sublattices with $a = 5.92$ Å, $b \approx 25(b_{\mathrm{TiS_2}}) \approx 31(b_{\mathrm{Hg}}) \approx 85.3$ Å, $c = 8.70$ Å, and $\beta = 96.5°$ can be used for the image simulations for the $\beta = 96.5°$ cell, and a unit with $a = 5.92$ Å, $b \approx 25(b_{\mathrm{TiS_2}}) \approx 31(b_{\mathrm{Hg}}) \approx 85.3$ Å, $c = 8.86$ Å, and $\beta = 102.3°$ can be used for the $\beta = 102°$ unit cell. Each of the atom positions in the unit cells were input individually, since the EMS software package cannot accommodate the sublattice symmetry of such incommensurate structures directly. Images were calculated for wide ranges of crystal thickness (1−32 unit cells) and defocus (200−700 Å underfocus) in narrow increments (~10−20 Å) in order to determine

Table 1. Parameters for the $\beta = 96.5°$ Structure Shown in Figure 7d

Unit-Cell Parameters

$a = 5.92$ Å; $b_{\mathrm{TiS_2}} = 3.41$ Å; $b_{\mathrm{Hg}} = 2.76$ Å; $c = 8.70$ Å, $\beta = 96.5°$

Atom Positions for the Two Interpenetrating *C*-Face-Centered Monoclinic Cells Described Using Space Group *C*2/*m*

atom	Wyckoff site	*x*	*y*	*z*
Ti	2(a)	0	0	0
S	4(i)	0.7	0	0.167
Hg[a]				
Hg[b]	2(a)	0	0	0

[a] The *x* and *z* coordinates of the two Hg atom columns along *b* corresponding to the Hg chains within the TiS$_2$ sublattice are (0,−,0.5) and (0.5,−,0.5). Since the *y* coordinates of the Hg positions are incommensurate with respect to the TiS$_2$ sublattice, no *y* coordinate is given for the Hg position in the TiS$_2$ sublattice. On average there are (3.41/2.76) = 1.24 Hg atoms per Ti atom along *b*. [b] Position of the Hg atom in its own sublattice

the best agreement with the experimental images. However, thin-region (<85 Å) *b* axis images cannot be simulated using such a large unit cell. In this case, simplified monoclinic unit cells were created based on the TiS$_2$ sublattice unit cells for the $\beta = 96.5°$ and 102° structures. Hg atoms were individually placed at (0,0,$^1/_2$) and ($^1/_2$,$^1/_2$,$^1/_2$) in the $\beta = 96.5°$ TiS$_2$ sublattice cell given in Table 1 and at ($^1/_4$,$^1/_4$,$^1/_2$) and ($^3/_4$,$^3/_4$,$^1/_2$) in the $\beta = 102°$ TiS$_2$ sublattice cell.[8] The symmetry of the *b*-axis projection of the structures is not influenced by this change in the *y* coordinates of the Hg positions. However, this change does reduce the Hg composition for these simulations from $x = 1.24−1.00$ for full occupancy of the Hg sites, as there are only two Hg positions in each unit cell.

The similarity of the $\beta = 96.5°$ and 102° structures is apparent in their indistinguishable *a*- and *b*-axis atomic projections, which yield two sets of interplanar distances and angles that are common to the two structures. As a result, these two structural modifications cannot be independently differentiated when viewed by HRTEM along their *a* and *b* axes. For example, Figure 8 shows a (*h*0*l*) image of a stage-1 region of a Hg$_x$TiS$_2$ crystal. As expected, the calculated images for the two structures were indistinguishable, with the images calculated for both structures providing excellent agreement with experiment. The inserts in Figure 8 show the calculated images for the $\beta = 96.5°$ and $\beta = 102°$ unit cells. The unit cell for each structure is shown as an inset.

However, *c*-axis SAD patterns and HRTEM images can be used to differentiate these two intercalate structures. Figure 9 shows a *c*-axis image of Hg$_x$TiS$_2$ that has been Fourier processed to remove the background noise associated with the diffuse scatter in the FFT. The calculated image for the $\beta = 96.5°$ structure in inset 1 shows excellent agreement with the experimental image, matching the strong one-dimensional modulation of the experimental image very well. Images were also calculated for different orientations of the $\beta = 102°$ structure as well as several other structures, including structures containing one or more empty guest galleries, in narrow increments over a wide range of thickness, defocus, and mercury composition using parameters similar to those given above. None of these images provided a reasonable match to the experimental images. In particular, none of the images for the $\beta = 102°$ structure were able to reproduce the

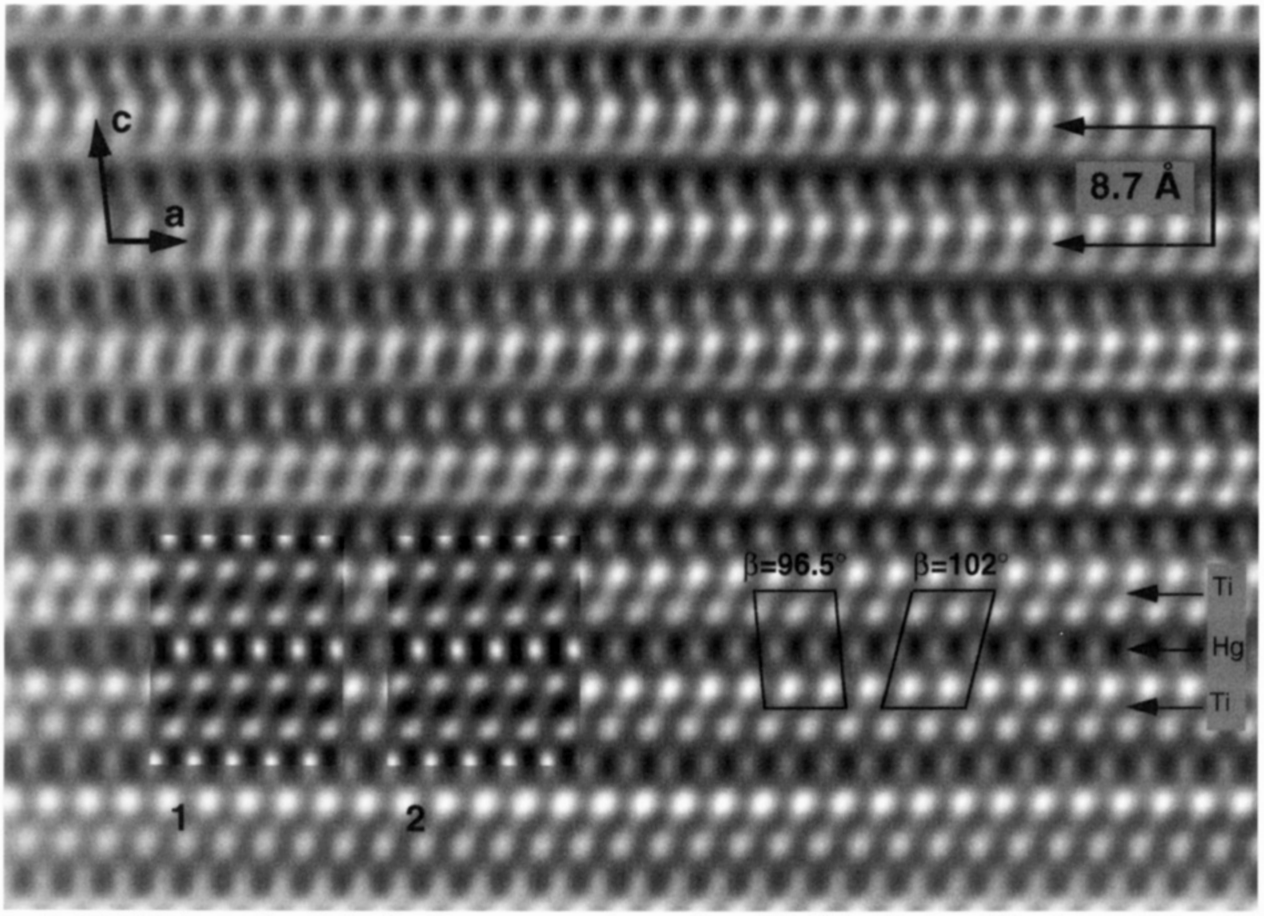

Figure 8. HRTEM image along b showing the commensurate $a-c$ plane of Hg_xTiS_2. The two different monoclinic unit cells corresponding to the $\beta = 96.5°$ and $\beta = 102°$ structures are outlined. The calculated images in the left (1) and right (2) insets are for the $\beta = 96.5°$ and $\beta = 102°$ structures, respectively (spherical aberration coefficient $C_s = 0.4$ mm, accelerating voltage $V = 200$ kV, defocus $\Delta_f = -620$ Å, specimen thickness $d = 14$ Å, and Hg site occupancy $n = 1.0$). The two structures are indistinguishable in this projection and give identical results in image simulations.

routinely observed strong one-dimensional 14.5 Å modulation seen in the experimental image in Figure 9. As a result, the best agreement attainable for the $\beta = 102°$ structure was quite poor, as shown in the second inset. In particular, the expected 14.5 Å modulation for the simulated $\beta = 102°$ image is very weak, which is generally characteristic of the $\beta = 102°$ image simulations. Further confirmation of the $\beta = 96.5°$ structure comes from the observed c-axis SAD patterns, which give d_{200} spacings of 2.94 ± 0.01 Å, in agreement with the value of 2.94 Å calculated for the $\beta = 96.5°$ structure. In contrast, the $\beta = 102°$ structure has a d_{200} spacing of 2.89 Å.[8] The reflections associated with the $\beta = 96.5°$ Hg_xTiS_2 SAD patterns persist throughout the deintercalation process until TiS_2 is formed. Therefore, Hg_xTiS_2 undergoes an intriguing structural transition from the $\beta = 102°$ to the $\beta = 96.5°$ structure early during the non-equilibrium deintercalation of Hg from $Hg_{1.24}$-TiS_2. Continued deintercalation results in regions of the $\beta = 96.5°$ Hg_xTiS_2 structure diminishing at the expense of the formation of regions of the host TiS_2 structure until the host structure is regenerated.

The calculated images for thin crystals having the $\beta = 96.5°$ structure were a clear function of mercury composition. However, slight differences in the Hg occupancy (e.g., $\Delta n = \pm 0.1$) could result in only modest changes in the agreement between the calculated and observed images, such as those shown in Figure 9. Thus, the stage-1 region observed in Figure 9 could contain a small number of guest–gallery vacancies within the Hg_xTiS_2 stage-1 composition region ($1.24 \geq x \geq 1.00$).[3]

The driving force for the structural transition from the $\beta = 102°$ structure to the $\beta = 96.5°$ structure is probably associated with the nonequilibrium deintercalation process. As discussed earlier, guest layers are routinely undergoing deintercalation during these studies, resulting in individual galleries that contain both intercalated and empty regions. Figure 10 shows an extreme example of the formation of such regions during deintercalation, where the contrast variations due to the presence of several Hg islands/guest-edge dislocations are visible. This c-axis image is of a relatively thin region of a Hg_xTiS_2 crystal with several galleries containing both intercalated and empty regions. The image has been Fourier filtered to remove the contribution from the TiS_2 host lattice in order to highlight the effect of the lamellar Hg islands/guest-edge dislocations on the image. Since related empty and intercalated gallery regions are generally present during deintercalation, the intercalate crystals need to accommodate the host-layer stacking arrangements for the intercalate and TiS_2 in the same crystal. As seen in Figure 7, host-layer stacking in the $\beta = 102°$ structure and TiS_2 differ by an interlayer displacement of about 2 Å [(1/3)a], whereas the displacement between the $\beta = 96.5°$ and TiS_2 structures is only about 1 Å [(1/6)a]. Thus, the strain energy associated with accommodating both the

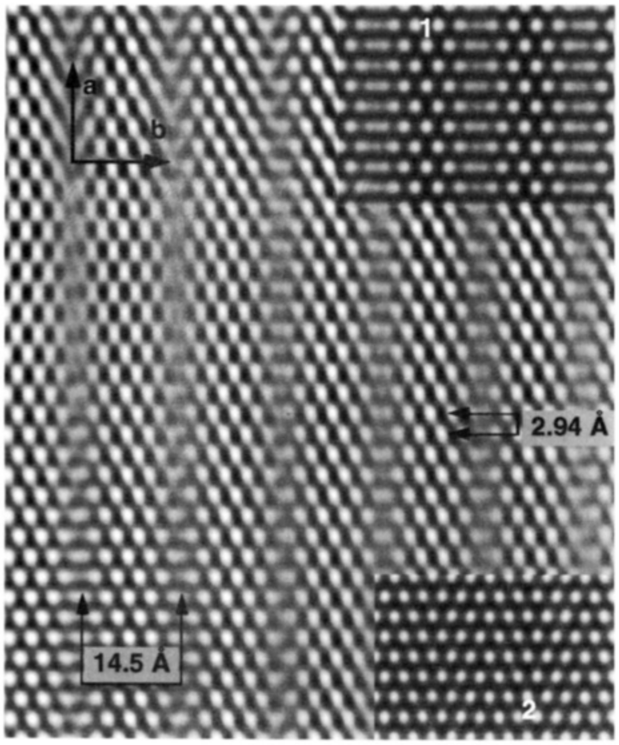

Figure 9. HRTEM image along *c* showing the partially commensurate *ab* plane. The calculated image shown in inset (1) is for a region of the $\beta = 96.5°$ structure containing three host layers ($C_s = 0.4$ mm, $V = 200$ kV, $\Delta_f = -660$ Å, and the Hg site occupancy is $n = 1.0$ for the two intercalated layers), which shows excellent agreement with the experimental image. Note the strong one-dimensional modulation of the images along *b*. The calculated image in inset (2) is the best agreement attainable for the $\beta = 102°$ structure, which is still poor ($C_s = 0.4$ mm, $V = 200$ kV, $\Delta_f = -600$ Å, and $n = 1.0$ for two guest layers in a region three host layers thick). Note the very weak one-dimensional modulation along *b*.

host and intercalate stacking arrangements in a gallery during deintercalation can be significantly reduced via the $\beta = 102°$ to $\beta = 96.5°$ phase transition. Furthermore, the transition should have a relatively low activation energy (E_a), as it can occur via a simple interlayer shift of the host layers along the Hg chain axis. In addition, the minimum host-layer restacking displacement that can be achieved for such an interlayer shift occurs for a (1/2)*b* shift. Therefore, the host-layer restacking process associated with mercury deintercalation can be viewed as a two-step process. First, shortly after deintercalation onset the host layers restack via an interlayer shift of (1/2)*b* resulting in the $\beta = 102°$ to $\beta = 96.5°$ phase transition. Second, as Hg deintercalation continues, the $\beta = 96.5°$ phase is converted to TiS_2 together with an interlayer shift of the host layers by (1/6*a*).

Unlike the HRTEM images taken along *b*, which are typically very well ordered, as shown in Figure 8, those along *a* were not nearly as well ordered, as shown in Figures 11a,b. This disorder can originate from (i) the incommensurate nature of the Hg chains along the *b* direction, (ii) the disorder in the Hg chains along *b*, which was observed by (*hk*0) SAD along *c*, and (iii) possible local host-layer stacking disorder. Although it is not possible to distinguish between the $\beta = 102°$ and $\beta = 96.5°$ structures via their separate *a*-axis images, as discussed previously, it is possible to detect the (1/2)*b* host-layer shift at the interface between lamellar regions of the two structures. Such (1/2)*b* shifts were observed in local regions of *a*-axis images, as shown in Figure 11, in further support of the (1/2)*b* transition from the $\beta = 102°$ to the $\beta = 96.5°$ structure. The projection of the host-layer Ti positions in Figure 12 demonstrates how the $\beta = 102°$ and $\beta = 96.5°$ structures can coherently coexist in the same crystal containing such (1/2)*b* stacking faults. It is likely that both the formation of the above stacking faults and the phase transition from $\beta = 102°$ to $\beta = 96.5°$ are assisted by thermally induced motion of the Hg chains along *b*.

Figure 13a shows a *c*-axis image that has been Fourier filtered to remove only low-frequency background noise and not the high-frequency background that can be associated with local structure modulations. Careful examination shows a slight *a*-axis modulation (≃0.2 Å) of the dark-contrast spots that correspond approximately to the Hg atom positions. By incorporating a similar modulation of the Hg atoms' *x* positions,

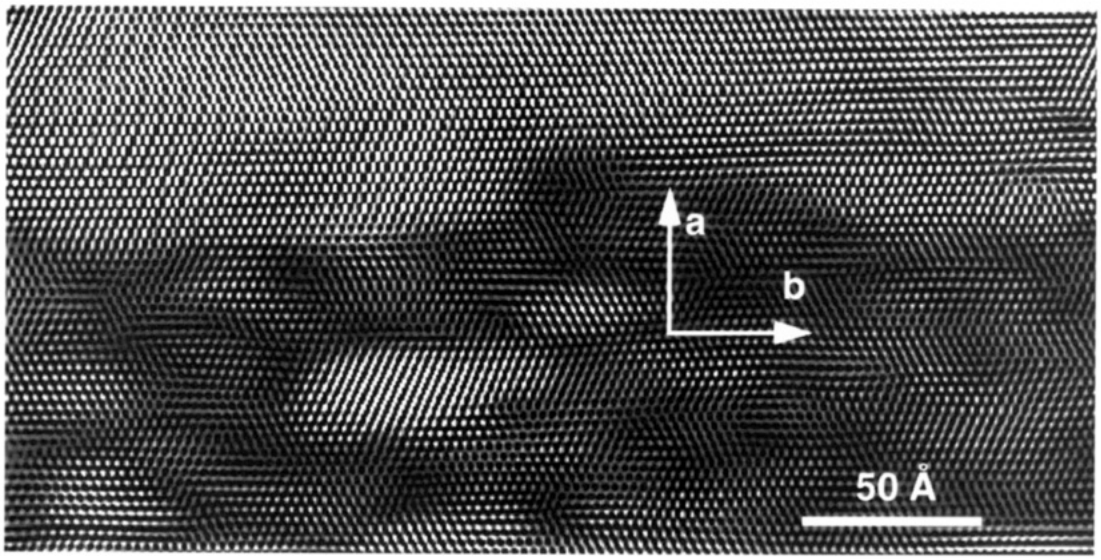

Figure 10. Fourier-processed HRTEM image along *c* taken from a region close to the edge of a Hg_xTiS_2 crystal. The TiS_2 sublattice has been filtered out leaving only the Hg sublattices. The areas of higher contrast correspond to regions of higher Hg content resulting from the presence of several Hg islands. The orientation of the subtracted host lattice is inset.

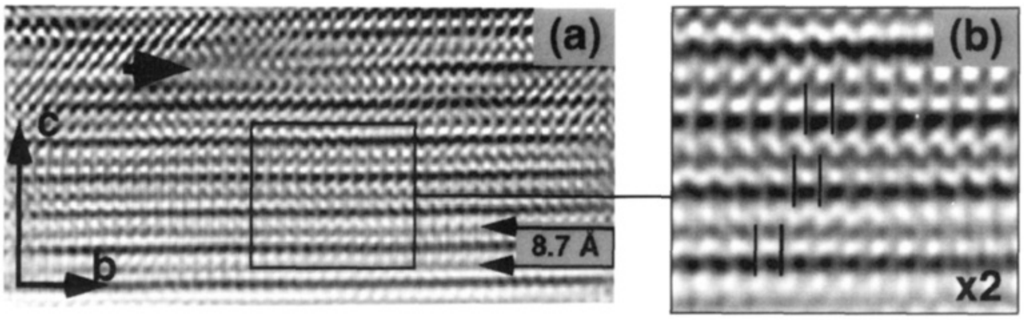

Figure 11. (a) HRTEM image of Hg_xTiS_2 along *a* showing substantial disorder in the partially commensurate *b*−*c* plane resulting from the incommensurate nature and the disorder of the Hg chains along *b*. One of the Hg layers is partially deintercalated, as shown by the large arrow, which indicates the horizontal dark black rows roughly correspond to the Hg guest layers. Ti layer positions are indicated by the smaller arrows. (b) Magnified section of the image in (a) showing ~(1/2)*b* shifts for some of the host layers consistent with the presence of (1/2)*b* stacking faults resulting from neighboring layers having the $\beta = 96.5°$ and $\beta = 102°$ structures. The vertical lines help identify the shifts. Such (1/2)*b* stacking faults are depicted schematically in Figure 12.

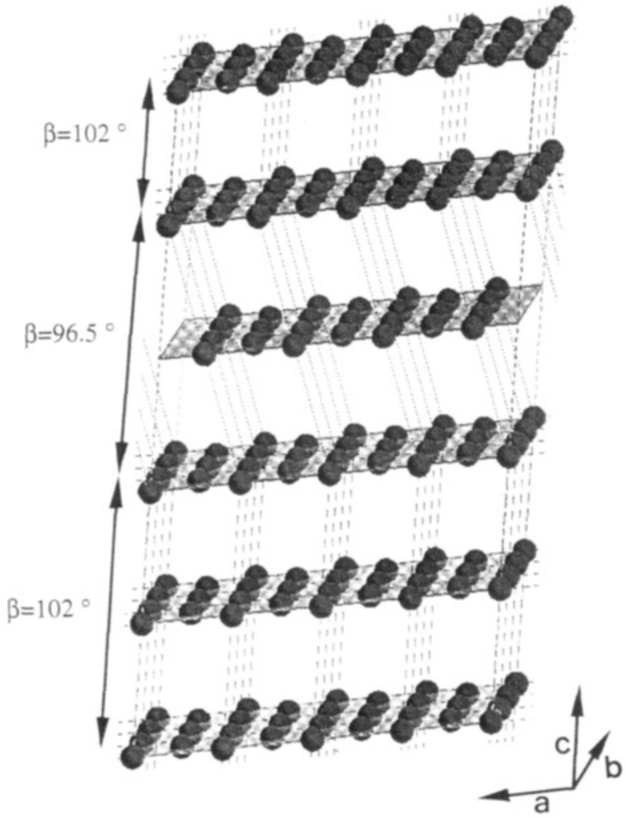

Figure 12. Schematic depiction of the coexistence of the $\beta = 102°$ and $\beta = 96.5°$ Hg_xTiS_2 structures with coherent (1/2)*b* host layer shifts between the structures. Only the Ti atom positions are shown. The third host layer from the top is displaced by (1/2)*b* producing two layers of the $\beta = 96.5°$ structure in the $\beta = 102°$ structure matrix.

with a period of 14.5 Å along *b*, into the image calculations for the $\beta = 96.5°$ structure, excellent agreement is obtained with the experimental image, as shown in Figure 13b. Thus, the Hg atom positions exhibit a slight modulation transverse to their chain axis which is induced by local guest-host interactions between the Hg and TiS_2 sublattices. Furthermore, simulated SAD patterns of this structure are in excellent agreement with observed SAD patterns, reproducing all of the observed reflections shown in Figure 2. In addition, the patterns demonstrate the array of extra diffraction spots that can be assigned to double diffraction in Figure 2 can also be generated directly by the presence of the Hg-sublattice modulations. The magnitude of these modulations, as well as this novel intercalate structure, is a direct consequence of the optimization of the guest−host interactions between the Hg and TiS_2 sublattices and the guest−guest (Hg−Hg) interactions combined.

An analogous *a*-axis modulation of the Hg chains apparently occurs in $Hg_{1.24}TiS_2$ as well, as indicated by (1) the invariance of χ^2 with the *x* position of the Hg chains for $0.27 \geq x \geq 0.23$ during its three-phase structure refinement, (2) the relatively high value observed for the $U_{1.1}$ thermal parameter compared with $U_{3.3}$ in its two-phase refinement, and (3) the fairly high value of χ^2 found for the refinement of the average structure of $Hg_{1.24}TiS_2$, where such sublattice−sublattice interactions could not be directly accommodated.[8] These modulations are also likely associated with the slight (~0.3%) expansion of the TiS_2 *a*-sublattice parameter from 5.90 to 5.92 Å in $Hg_{1.24}TiS_2$.[8] Thus, complete descriptions of the $\beta = 102°$ and $\beta = 96.5°$ structures require (3 + 1) dimensional space groups due to the *a*-axis modulation of the Hg sublattice by the host sublattice. Although similar off-chain-axis modulations have also been reported for the infinite incommensurate Hg chains in $Hg_{3-\delta}MF_6$,[15] the above HRTEM observations provide the most direct evidence to date in support of the applicability of superspace theory to such systems.

Conclusions

This investigation has demonstrated that intercalated Hg in Hg_xTiS_2 is arranged in infinite one-dimensional chains during nonequilibrium deintercalation. The Hg_xTiS_2 structure formed during deintercalation can be described as two interpenetrating monoclinic Hg and TiS_2 sublattices having commensurate *a* and *c* axes and a common angle *β*, which are incommensurate along their common *b* axis. The 2-fold intralayer symmetry of the Hg sublattice and the 3-fold intralayer symmetry of the host sublattice results in the formation of three equivalent Hg sublattices that are rotated by 120° relative to each other. The same Hg sublattice orientations are grouped together in nearby layers, indicating that neighboring Hg sublattice layers with the same orientation are thermodynamically stable. The different orientations of the Hg sublattice in a crystal are probably a consequence of their nucleation at different sites at the crystal edges during intercalation. Moreover, the Hg−Hg bonding along the guest chains dominates the guest−guest interactions, as evidenced by the relatively short intrachain Hg−Hg distance of

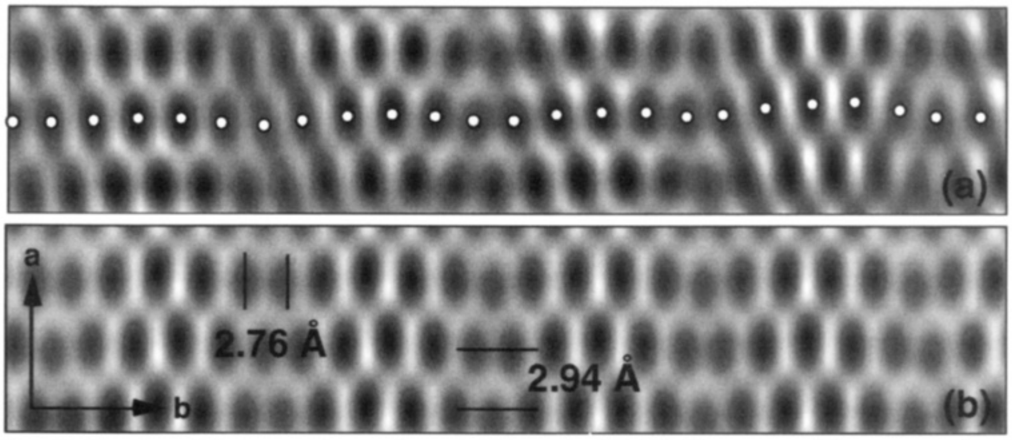

Figure 13. (a) Magnified region of the image along *c* shown in Figure 6a. The black spots roughly correspond to the Hg positions. Note the wavelike nature of the Hg chains corresponding to a modulation of the *x* coordinates of the Hg positions. The white spots highlight the modulation of the chains. The image is selectively magnified by 30% along the *a* direction to emphasize the modulation. (b) Simulated image incorporating a ±0.2 Å modulation of the *x* coordinates of Hg positions that shows the same modulated appearance as in (a). ($C_s = 1.2$ mm, $V = 400$ kV, $\Delta_f = -540$ Å, and $n = 1.0$ for six guest layers in a region seven host layers thick).

2.76 Å compared to the interchain Hg–Hg distance of 3.27 Å. These compounds also have significant guest–host interactions between the Hg chains and the sulfur channels in which they reside. In particular, these interactions manifest themselves in the slight off-chain-axis modulation of the Hg positions, with the observed modulated structure resulting from the optimization of the local Hg–S and Hg–Hg interactions.

The Hg chains in Hg_xTiS_2 exhibit thermally activated disorder along their chain-axis (*b*) direction, which suggests that deintercalation is primarily associated with the motion of the Hg chains along the chain axis. Thus, the reaction processes in Hg_xTiS_2 are primarily one-dimensional in character, unlike other M–TMDICs whose reaction chemistry is generally a two-dimensional process.[10,11] The ease of Hg motion along *b* is also likely correlated with the formation of the observed structure, which has sulfur channels that offer DTAP coordination of the Hg chains. This structure is derived during Hg deintercalation from the equilibrium $Hg_{1.24}TiS_2$ structure[8] by host-layer restacking along the Hg-chain axis. The restacking process amounts to a simple (1/2)*b* sliding of the host layers, which transforms the coordination of the sulfur channels about the Hg chains from trigonal prismatic to DTAP, with the formation of the observed $\beta = 96.5°$ Hg_xTiS_2 structure. Continued Hg deintercalation results in the formation and growth of regions of TiS_2 at the expense of the regions containing the $\beta = 96.5°$ structure until TiS_2 is formed.

The complementary study of the complex structures formed by Hg_xTiS_2 by HRTEM in the present paper and by X-ray diffraction in the preceding paper has provided a detailed structural understanding of Hg_xTiS_2 intercalation compounds that could not have been achieved by either technique alone. HRTEM provides an atomic-level view of the structure, with the ability to elucidate such features as individual sublattice orientations, local crystal disorder, and local structural modulation of atomic positions. In situ HRTEM also allows observation of the structure at different stages of the deintercalation process itself. However, HRTEM is unable to probe fully intercalated $Hg_{1.24}TiS_2$ (due to Hg loss), can only provide nonequilibrium information for Hg_xTiS_2 and does not allow for the complete refinement of observed structure(s). All of these HRTEM shortcomings can be overcome by X-ray diffraction. Therefore, the combination of HRTEM and X-ray diffraction provides a powerful dual approach to the investigation of complex structural arrangements, such as those found in Hg_xTiS_2.

Acknowledgment. We wish to acknowledge the National Science Foundation for support through Grants DMR 91-06792 and INT-8914990, and acknowledgment is made to the donors of The Petroleum Research Fund, administeted by the American Chemical Society, for partial support of this research. The electron microscopy was conducted at the Center for High Resolution Electron Micropscopy at Arizona State University supported by NSF Grant DMR-9115680. We also wish to thank the Center for Solid State Science for use of its Materials Preparation Facility and J. M. Cowley for helpful discussion. It is a pleasure to thank Prof. J. Rouxel for his continuous interest and support. This work was also supported by a Conseil Régional des Pays de la Loire grant (P.G.).

CM940489T